

Supporting Information

for *Laser Photonics Rev.*, DOI 10.1002/lpor.202500032

Computational Adaptive Optics for Fluorescence Microscopy via Sparse Blind Deconvolution

*Runnan Zhang, Heheng Du, Ning Zhou, Zihao Zhou, Hanci Tang, Jiaming Qian, Qian Chen
and Chao Zuo**

Computational Adaptive Optics for Fluorescence Microscopy via Sparse Blind Deconvolution: Supporting Information

Runnan Zhang^{1,2,3,†}, **Heheng Du**^{1,2,3,†}, **Ning Zhou**^{1,2,3,†}, **Zihao Zhou**^{1,2,3}, **Hanci Tang**^{1,2,3},
Jiaming Qian^{1,2,3}, **Qian Chen**^{1,3}, and **Chao Zuo**^{1,2,3,*}

¹Smart Computational Imaging Laboratory (SCILab), School of Electronic and Optical Engineering, Nanjing University of Science and Technology, Nanjing, Jiangsu 210094, China

²Smart Computational Imaging Research Institute (SCIRI) of Nanjing University of Science and Technology, Nanjing, Jiangsu 210019, China

³Jiangsu Key Laboratory of Spectral Imaging & Intelligent Sense, Nanjing University of Science and Technology, Nanjing, Jiangsu 210094, China

[†]Runnan Zhang, Heheng Du and Ning Zhou contributed equally to this work.

*Address all correspondence to Chao Zuo, zuochao@njust.edu.cn

ABSTRACT

This document provides supplementary information for “Computational Adaptive Optics for Fluorescence Microscopy via Sparse Blind Deconvolution: Supporting Information”.

Contents

Supporting Information S1. Blind Deconvolution Theory.

Supporting Information S2. Blurred kernel estimate using Sparse prior.

Supporting Information S3. Impact of Convolution Kernel Size on Reconstruction Performance.

Supporting Information S4. Using sparse prior knowledge improves imaging resolution and contrast.

Supporting Information S5. Supplemental experiments under confocal laser scanning microscope.

Supporting Information S6. Execution Time Evaluation Under Different Conditions.

Supporting Video S1: CAO-SBD method for BPAEC under wide-field fluorescence microscope.

Supporting Video S2: CAO-SBD method for BPAEC under confocal laser scanning microscope.

Supporting Video S3: Supplementary experiments of CAO-SBD method for BPAEC under confocal laser scanning microscope.

Supporting Information S1. Blind Deconvolution Theory

In the traditional Richardson-Lucy Deconvolution (RLD) algorithm^{1,2}, the method is based on Maximum Likelihood Estimation (MLE)³. The RLD algorithm aims to recover the original, un-blurred image from a blurred observation by maximizing the likelihood of the observed data given the model parameters. Given a blurred image as the observed data, the algorithm attempts to minimize the difference between the blurred and true images by maximizing the likelihood. The RLD algorithm assumes that the observed data are the result of the convolution of the true image with the Point Spread Function (PSF) and the addition of noise⁴. The algorithm seeks to find the best image estimate by maximizing the likelihood function, which measures the probability of the observed data given the model parameters but does not directly consider the prior probability distribution of the image.

Maximum A Posteriori Estimation (MAP) incorporates prior knowledge into the estimation process, taking into account the prior probability distribution of the parameters. MAP estimation can be viewed as MLE with a regularization term that leverages additional information to improve the estimation results.

In blind deconvolution, one observes a blurred image $g(x,y)$ which is the convolution of a latent sharp image $f(x,y)$ with a latent blur kernel $h(x,y)$, corrupted by measurement noise $n(x,y)$:

$$g(x,y) = f(x,y) * h(x,y) + n(x,y) \quad (\text{S1})$$

For brevity in subsequent derivations, we hereafter abbreviate $g(x,y)$, $f(x,y)$, $h(x,y)$, $n(x,y)$ as g , f , h and n , we denote the number of unknowns in $f(x,y)$, $h(x,y)$ by N , M respectively, where typically $M \ll N$. Formulate the problem in derivative space, and consider:

$$f_h * g = h * (f_h * f) + n_h, f_v * h = h * (f_v * f) + n_v \quad (\text{S2})$$

where $\{f_h, f_v\} = \{|-1, 1|, |-1, 1|^T\}$. The “blurred input” is taken as $g = [f_h * g; f_v * g]$, and one solves for the derivative image $f = [f_h * f; f_v * f]$

Supporting Information S2. Blurred kernel estimate using Sparse prior

Our goal is to estimate $f(x,y)$ and $h(x,y)$ from the blurred input y . Since there are many pairs f, h which can explain the $g(x,y)$ observation, one should utilize some prior knowledge. Leveraging prior knowledge from natural image statistics, particularly the sparsity of the derivative distribution in fluorescence imaging. In this article, we express the sparse prior as a mixture of J Gaussians (MOG):

$$p(f) = \prod_i \prod_\gamma \rho(f_{i,\gamma}(f)) \quad (\text{S3})$$

$$\rho(f_{i,\gamma}(f)) = \sum_j \frac{\pi_j}{\sqrt{2\pi}\rho_j} e^{-\frac{1}{2\sigma_j^2} \|f_{i,\gamma}(f)\|^2} \quad (\text{S4})$$

where $f_{i,\gamma}(f)$ denotes the output of $f_\gamma(f) * f$ at the i 'th pixel. In the image space formulation Eq. S1, $\{f_\gamma\}_{\gamma=1}^J$ are a set of derivative filters. In the derivative space formulation Eq. S2, $\{f_\gamma\}$ consists of the delta filter.

For the simplicity of the derivation, we consider here a uniform prior on $h(x,y)$ and only enforce all entries of $h(x,y)$ to be non-negative.

Assuming a Gaussian imaging noise with variance η^2 , we can write

$$p(g|f, h) = \frac{1}{(\sqrt{2\pi}\eta)^N} e^{-\frac{\|h * f - g\|^2}{2\eta^2}} \quad (\text{S5})$$

where N is the number of image pixels. Combining Eq. S3-S5 we express $p(g, f, h) = p(g, f|h)p(h) = p(g|f, h)p(f)p(h)$.

The straightforward approach to blind deconvolution is to search for the MAP solution⁵: since the kernel size is significantly smaller than the image size, a MAP estimation of the kernel alone is well-conditioned. Thus, one should look for a MAP estimate, marginalizing over all latent images:

$$\begin{aligned} h &= \arg \max p(h|g) = \arg \max p(g|h) \\ p(g|h) &= \int p(f, g|h) df \end{aligned} \quad (\text{S6})$$

However, computing the integral of Eq. S6 is not trivial, and we will discuss approximation strategies.

We solve for the best kernel given the image. However, it accounts for the covariance around the image estimate and not only for the mean image estimate itself. Formally, the algorithm is defined as follows:

Step 1. Set $q(f) = p(f|g, h)$ and compute μ, C , the mean and covariance of $q(f)$, which are the mean image given a kernel and the surrounding covariance.

Step 2. Find $h(x,y)$ minimizing

$$\hat{h}(x,y) = \arg \min_{h(x,y)} [\|f(x,y) \otimes h(x,y) - g(x,y)\|^2] \quad (\text{S7})$$

Approximation strategies: Since Eq. S7 integrates a quadratic term, the mean and covariance computed in Step 1 are sufficient statistics of $q(f)$ required for that minimization. By solving a quadratic programming problem. This requires knowledge of the mean and covariance of q alone and not the full distribution.

Eq. S7 is minimized by the solution to the quadratic programming problem

$$\hat{h}(x, y) = \arg \min_{h(x, y)} \frac{1}{2} h^T(x, y) A_h^T h(x, y) - b_h^T h(x, y) \quad (\text{S8})$$

where

$$A_h(i_1, i_2) = \sum_i \mu(i + i_1) \mu(i + i_2) + C(i + i_1, i + i_2) \quad (\text{S9})$$

$$b_h(i_1) = \sum_i \mu(i + i_1) g(i) \quad (\text{S10})$$

If $h(x, y)$ is an $m \times m$ kernel and $M = m^2$, A_h is an $M \times M$ matrix representing the covariance of all $m \times m$ windows in $f(x, y)$, and b_h the correlation with $g(x, y)$:

$$A_k(i_1, i_2) = \sum_i x(i + i_1) x(i + i_2), b_k(i_1) = \sum_i x(i + i_1) y(i) \quad (\text{S11})$$

where i sums over all image pixels, and i_1, i_2 are kernel indexes. Averaging Eq. S11 over x values coming from the distribution $q(f)$ provides Eq. S9 and Eq. S10. Therefore, minimizing Eq. S7 with respect to h is equivalent to minimizing Eq. S8.

Since the mean and covariance cannot be computed in closed form for a sparse prior, we approximate the conditional distribution with a simpler one using variational optimization.

Given h it solves a nonblind deconvolution problem, at which a mean latent image estimate μ is computed using iterative reweighted least squares. In each iteration, one finds μ by solving an $N \times N$ linear system $A_x \mu = b_x$. This system seeks μ minimizing the convolution error plus a weighted regularization term on the derivatives^{6,7}. The weights are selected to provide a quadratic upper bound on the MOG negative log-likelihood based on the previous μ solution. To efficiently compute the covariance around the mean image μ , we approximate it with a diagonal matrix. The diagonal approximation can be computed easily in $O(N)$, by inverting the diagonal elements of the weighted deconvolution system A_x .

Supporting Information S3. Impact of Convolution Kernel Size on Reconstruction Performance.

The selection of convolution kernel size presents a crucial consideration between computational accuracy and the speed of initial PSF estimation. Classical non-blind deconvolution methodologies, including RL Deconvolution and Wiener Deconvolution (WD), fundamentally rely on exact a priori knowledge of the PSF. Empirical evidence confirms that these algorithms attain peak performance exclusively when the supplied PSF perfectly aligns with the imaging system's intrinsic degradation characteristics. Consequently, within blind deconvolution where PSF estimation becomes an integral component. To achieve an optimal choice, the size of the convolution kernel must closely match the spatial distribution characteristics of the theoretical PSF. In optical systems exhibiting aberrations, where prior knowledge of aberration magnitude is unavailable, our method employs the computationally derived theoretical PSF dimensions as a reference benchmark to estimate the system's PSF.

In incoherent imaging systems, the spatial resolution of the theoretical PSF is constrained by the diffraction limit. The corresponding cutoff frequency of the Optical Transfer Function (OTF) is determined by system parameters, which can be expressed as $f_c = 2NA/\lambda$ (where NA is the numerical aperture and λ is the illumination wavelength). When the estimated PSF kernel exhibits excessive spatial extension, it leads to significant contraction of the OTF's effective support domain in the frequency domain. This phenomenon causes systematic loss of high-frequency information, forcing the imaging system to retain only low-frequency spatial components of the specimen. Notably, when the spatial scale of the practically estimated PSF is smaller than theoretical predictions (i.e., the kernel size fails to meet diffraction-limited requirements), it creates unique information reconstruction issues during deconvolution. This dimensional mismatch causes algorithms to misinterpret high-frequency artifacts that should belong to PSF sidelobes as genuine specimen structures. Specifically, undersized estimation kernels introduce high-frequency noise components that should have been suppressed, triggering amplification of spurious frequency components during deconvolution. This ultimately results in non-physical ringing artifacts and detail distortion in reconstructed images.

The Airy disk represents the diffraction limit of an optical system's imaging response to an ideal point source. In incoherent fluorescence imaging, the spatial distribution of the ideal PSF essentially equates to the intensity distribution of the Airy disk, described by the Airy function, which can be mathematically expressed as: $I(r) \propto \left[\frac{2J_1(kr \sin \theta)}{kr \sin \theta} \right]^2$

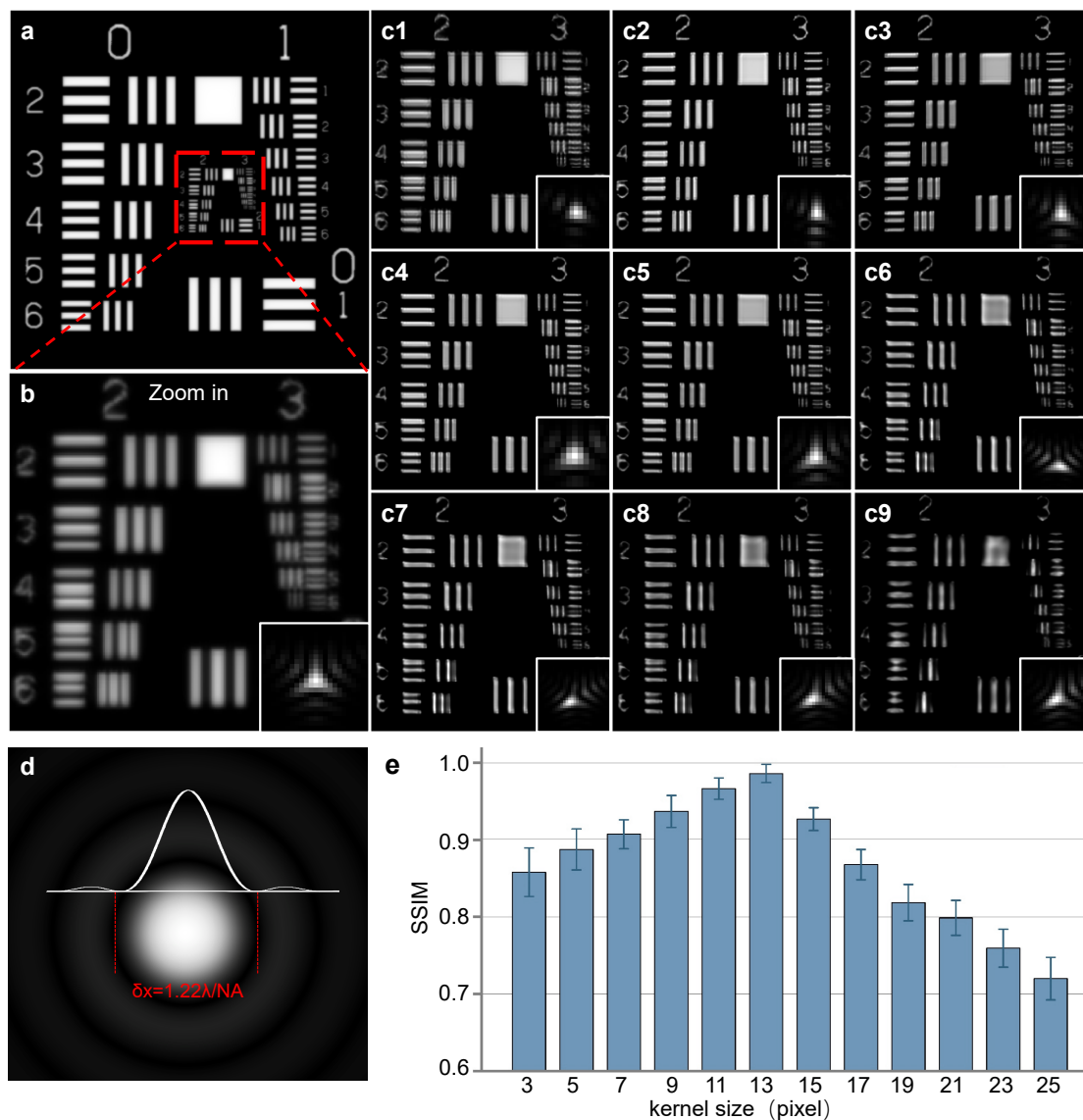
$$I(r) \propto \left[\frac{2J_1(kr \sin \theta)}{kr \sin \theta} \right]^2 \quad (\text{S12})$$

where, $J_1(x)$ is the first-order Bessel function of the first kind, k is the wavenumber, r is the radial distance, and θ is the angle of incidence. As shown in Fig. S1d, The first zero of the Bessel function corresponds to the central lobe of the Airy disk, which contains approximately 83.8% of the light intensity. The diameter of the lobe at the first intensity null is given by the following equation: $D_{\text{Airy}} = 2r_{\text{Airy}} = 1.22\lambda/NA$. The second zero-crossing point (1.83 times the central radius)

encompasses 91% of the energy.

To mitigate the loss of high-frequency sample information caused by an excessively large PSF kernel estimation and the erroneous attribution of high-frequency artifacts (originating from PSF sidelobes) to actual specimen structures when the kernel is undersized, we select the second zero-crossing point as the benchmark for designing the convolution kernel. In a typical wide-field fluorescence system ($NA = 0.6$, $\lambda = 532nm$, $pixelsize = 6.5/40\mu m$), calculations yield a theoretical optimal kernel size of 13×13 pixels, ensuring that the kernel size can fully characterize the spatial attenuation characteristics of the PSF while avoiding increasing computational complexity.

In Supplementary Fig. S1, we validate the above conclusions through systematic simulation experiments by conducting wide-field fluorescence imaging of 1024×1024 USAF target (with experimental parameters consistent with those in the main text for the wide-field fluorescence experiment). Experimental results indicate that when the kernel size is smaller than the theoretical value, as shown in Fig. S1c1 (7×7 kernel) and Fig. S1c2 (9×9 kernel), undersized PSF estimation kernels introduce high-frequency noise components that should have been suppressed, leading to erroneous attribution of high-frequency artifacts (inherent to PSF sidelobes) to genuine specimen structures. Conversely, an excessively large kernel size, such as in Fig. S1c6 (19×19 kernel), while to some extent able to reflect the spatial characteristics of the PSF, excessively extended PSFs cause significant contraction of the OTF's effective support domain in the frequency domain, resulting in systematic loss of high-frequency information during image reconstruction and introduces computation time, resulting in reduced estimation accuracy and rapid and significant deterioration in image quality. Notably, kernels close to the size of the theoretical PSF, such as those in Fig. S1c4 (13×13 kernel) and Fig. S1c5 (15×15 kernel), achieve optimal imaging results while maintaining computational efficiency, validating the effectiveness of the theoretical predictions.



Supporting Information S4. Using sparse prior knowledge improves imaging resolution and contrast

In fluorescence imaging, the convolution of the object with the smaller PSF always confers relative sparsity⁸. Therefore, we propose introducing sparsity as another prior knowledge to extract the fluorescent object's high-frequency information⁹.

Respectively, we utilized images with sparse and non-sparse distributions and convolved these ground-truth structures with PSFs of varying sizes to simulate the images detected by microscopes with different spatial resolutions. We observed that our estimation was more effective for images with high sparsity. However, if the samples did not fulfill the sparsity condition, the estimation might incur some errors, as demonstrated by examples in Fig. S2. In Fig. S2, the processing results of our method on strongly sparse images, relatively sparse images, and weakly sparse images are displayed, all with 50 iterations. It can be observed that our method performs better when dealing with strongly sparse images, providing more accurate estimations of both the PSF and the image, making it suitable for fluorescence imaging.

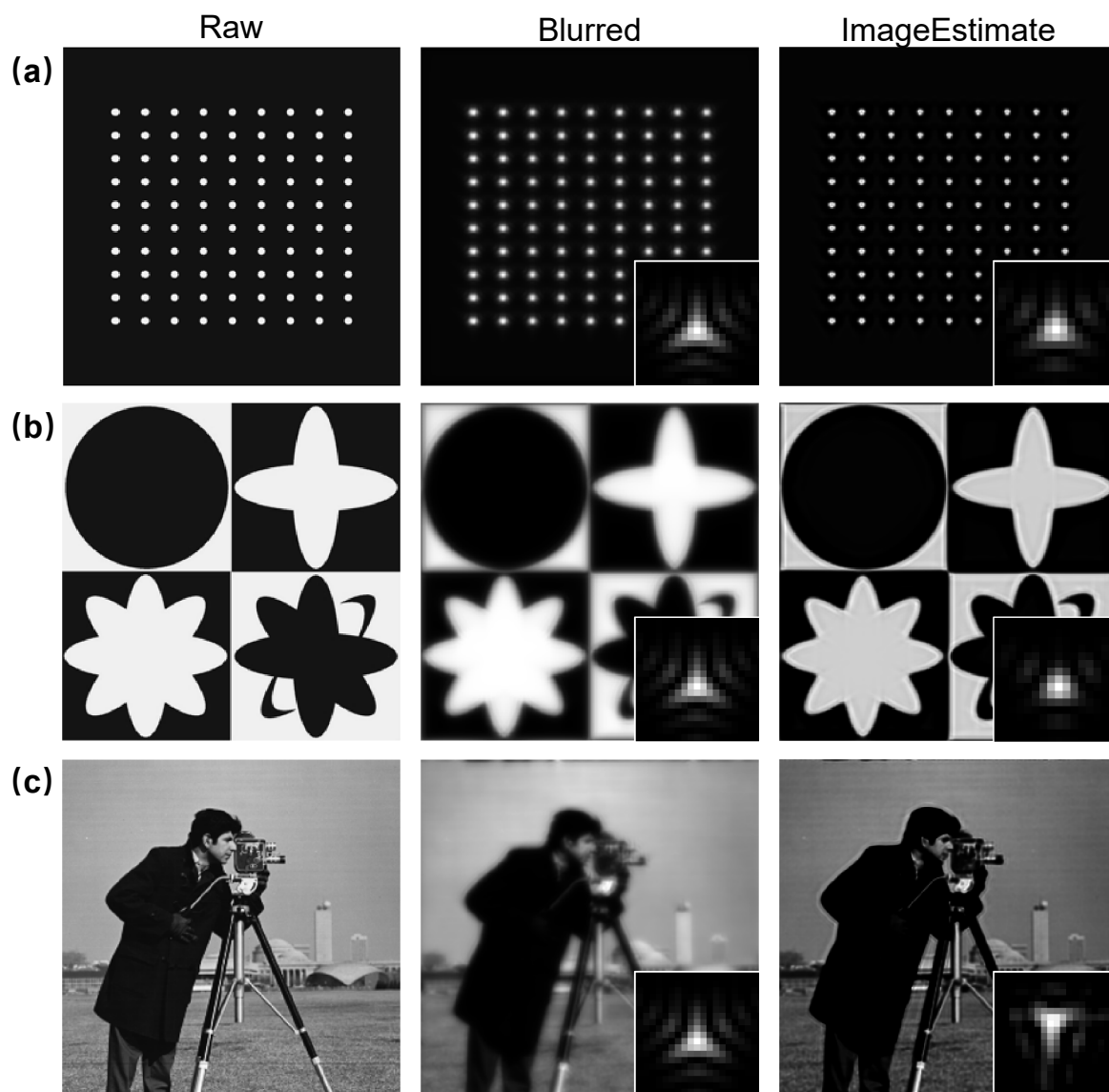


Figure S2. Reconstruction of images with varying sparsity. a-c) The sparsity decreases sequentially. The first column shows the input original images, The bottom right corner shows the simulated PSF, the second column displays the blurred images, the last column presents our deconvolution results, and the bottom right corner of the figure shows the estimated PSF.

Supporting Information S5. Supplemental experiments under confocal laser scanning microscope

To evaluate the performance of our blind deconvolution method and to verify its robustness, we conducted multiple experiments on BAPEC to validate the performance and robustness of our approach, as shown in Fig. S3 and S4.

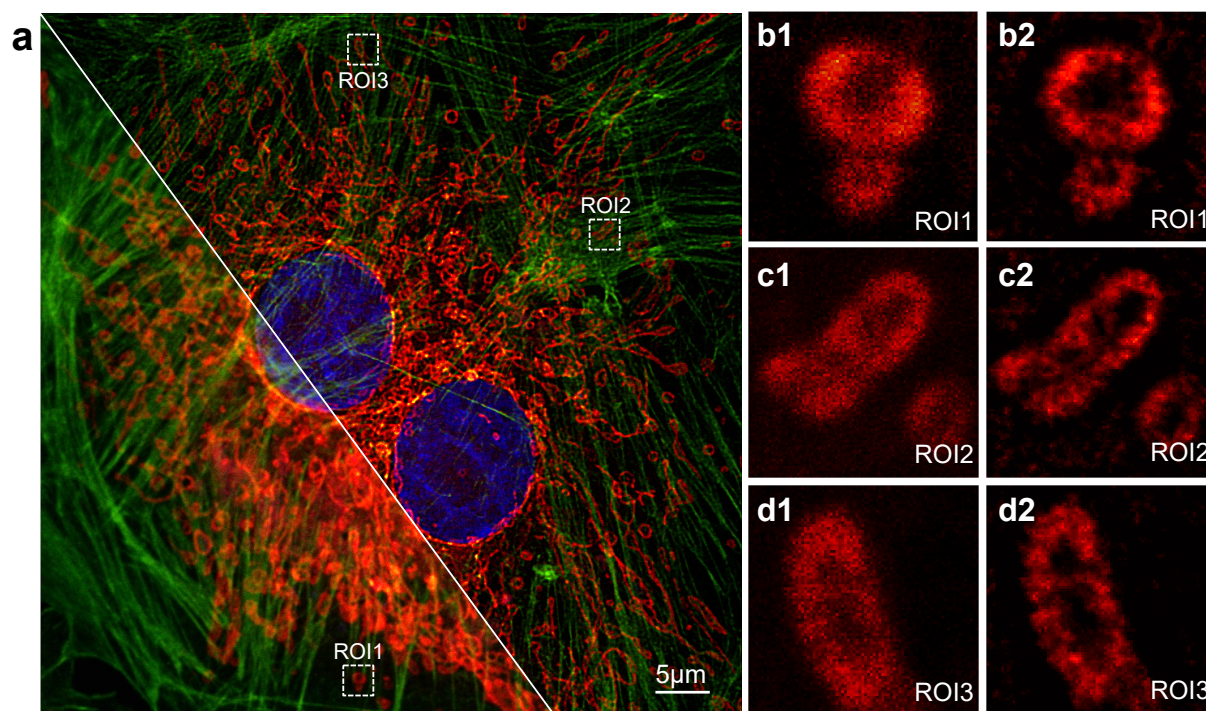


Figure S3. Supplementary experiment 1 of confocal laser scanning microscopy on BAPEC. a) The merged result of the three channels. b-d) Enlarged regions of mitochondria of BAPEC labeled with MitoTracker™ Red CMXRos, b1-d1 are the captured original images, and b2-d2 are the results of CAO-SBD.

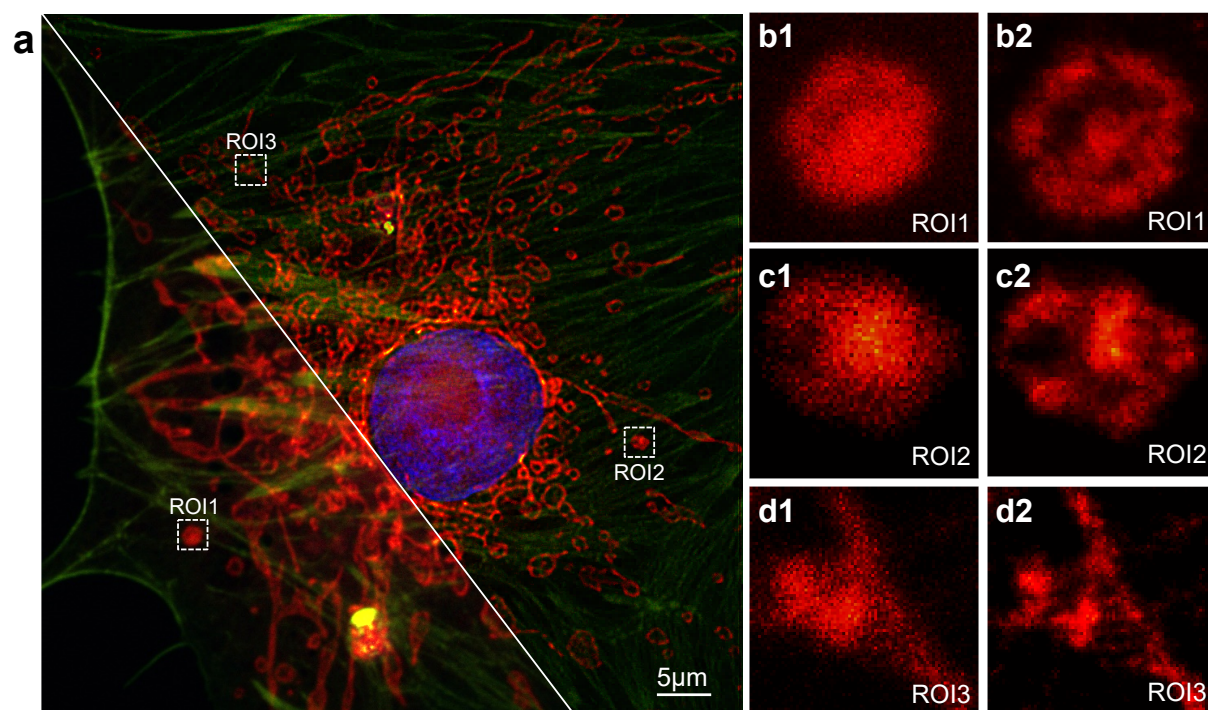


Figure S4. Supplementary experiment 2 of confocal laser scanning microscopy on BAPEC. a) The merged result of the three channels. b-d) Enlarged regions of mitochondria of BAPEC labeled with MitoTracker™ Red CMXRos, b1-d1 are the captured original images, and b2-d2 are the results of CAO-SBD.

Supporting Information S6. Execution Time Evaluation Under Different Conditions.

During the kernel estimation process, we innovatively implemented acceleration through CUDA parallel computing architecture (hardware platform: NVIDIA RTX 4060 GPU). As shown in table S1, comparative performance evaluations among MATLAB native implementation, C++ baseline, and CUDA-accelerated C++ versions demonstrate that under typical experimental conditions with a theoretical PSF size of 13×13 pixels, our CUDA-based parallel optimization reduces the total processing time for estimating convolution kernels from single-frame blurred images to 17 seconds. Particularly noteworthy is our dedicated acceleration framework developed for the blind deconvolution algorithm – achieving 50 iterations of deconvolution processing for high-resolution 2048×2048 pixel images in merely 24.9 seconds, representing significant computational efficiency improvements over conventional implementations.

Table S1. Algorithmic Runtime Profiling and Parallel Acceleration Benchmark.

Platform	Matlab		C++		C++(CUDA)	
Efficiency	Time	Memory	Time	Memory	Time	Memory
Tabel 1. Convolution Kernel Estimate.						
Kernel (7×7)	58s	4.71GB	107s	3.47GB	9s	3.13GB
Kernel (13×13)	155s	5.24GB	308s	4.78GB	17s	4.71GB
Kernel (25×25)	361s	6.62GB	783s	5.14GB	32s	4.89GB
Tabel 2. Blind Deconvolution (50 iterations).						
Image (512×512)	24s	4.33GB	61s	1.73GB	2.55s	1.30GB
Image (1024×1024)	97s	4.68GB	337s	2.28GB	10s	2.13GB
Image (2048×2048)	308s	5.29GB	965s	3.93GB	24.9s	3.71GB

References

1. Goodman, J. W. Introduction to Fourier optics (Roberts and Company publishers, 2005).
2. Lucy, L. B. An iterative technique for the rectification of observed distributions. *Astron. Journal*, Vol. 79, p. 745 (1974) 79, 745 (1974).
3. Holmes, T. J. Blind deconvolution of quantum-limited incoherent imagery: maximum-likelihood approach. *JOSA A* 9, 1052–1061 (1992).
4. Holmes, T. J. et al. Light microscopic images reconstructed by maximum likelihood deconvolution. *Handb. biological confocal microscopy* 389–402 (1995).
5. Levin, A., Weiss, Y., Durand, F. & Freeman, W. T. Understanding and evaluating blind deconvolution algorithms. In 2009 IEEE conference on computer vision and pattern recognition, 1964–1971 (IEEE, 2009).
6. Richardson, W. H. Bayesian-based iterative method of image restoration. *JOSA* 62, 55–59 (1972).
7. Engl, H. Regularization of inverse problems. *Math. its Appl.* 375 (1996).
8. Born, M. & Wolf, E. Principles of optics: electromagnetic theory of propagation, interference and diffraction of light (Elsevier, 2013).
9. Pawley, J. Handbook of biological confocal microscopy. Springer google schola 2, 1035–1040 (2006).